
PHYSICS-INFORMED TIME-INTEGRATED DEEPONET: TEMPORAL TANGENT SPACE OPERATOR LEARNING FOR HIGH-ACCURACY INFERENCE

Luis Mandl

Institute of Structural Mechanics and Dynamics in Aerospace Engineering, University of Stuttgart;
Experimental Hepatobiliary Surgery Group,
Department of Hepatobiliary Surgery and Visceral Transplantation,
University of Leipzig Medical Center;
Department of Civil and Systems Engineering,
Johns Hopkins University
luis.mandl@isd.uni-stuttgart.de

Dibyajyoti Nayak

Department of Civil and Systems Engineering,
Johns Hopkins University
dnayak2@jh.edu

Tim Ricken

Institute of Structural Mechanics and Dynamics in Aerospace Engineering, University of Stuttgart
tim.ricken@isd.uni-stuttgart.de

Somdatta Goswami

Department of Civil and Systems Engineering,
Johns Hopkins University
somdatta@jhu.edu

ABSTRACT

Accurately modeling and inferring solutions to time-dependent partial differential equations (PDEs) over extended temporal horizons remains a core challenge in scientific machine learning. Traditional full rollout (FR) methods, predicting entire trajectories in a single pass, often fail to capture the causal dependencies inherent to dynamical systems and exhibit poor generalization outside the training time horizon. In contrast, autoregressive (AR) approaches, which evolve the system step by step, are prone to error accumulation, as predictions at each time step depend on potentially erroneous prior outputs. These shortcomings limit the long-term accuracy and reliability of both strategies. To overcome these issues, we introduce Physics-Informed Time-Integrated Deep Operator Network (PITI-DeepONet), an operator learning framework designed for stable and accurate long-term time evolution, well beyond the training time horizon. PITI-DeepONet employs a dual-output DeepONet architecture trained via either fully physics-informed or hybrid physics- and data-driven objectives. The training enforces consistency between the learned temporal derivative and its counterpart obtained via automatic differentiation. Rather than directly forecasting future states, the network learns the time-derivative operator from the current state, which is then integrated using classical time-stepping schemes - such as explicit Euler, fourth-order Runge-Kutta, or second-order Adams-Basforth-Moulton - to advance the solution sequentially in time. Additionally, the framework can leverage residual monitoring during inference to estimate prediction quality and detect when the system transitions outside the training domain. Applied to benchmark problems, PITI-DeepONet demonstrates enhanced accuracy and stability over extended inference time horizons when compared to traditional methods. Mean relative \mathcal{L}_2 errors reduced by 84% (versus FR) and 79% (versus AR) for the one-dimensional heat equation; by 87% (versus FR) and 98% (versus AR) for the one-dimensional Burgers equation; and by 42% (versus FR) and 89% (versus AR) for the two-dimensional Allen-Cahn equation. By moving beyond classic FR and AR schemes, PITI-DeepONet paves the way for more reliable, long-term integration of complex, time-dependent PDEs.

1 Introduction

Neural operators (NOs) have emerged as powerful surrogate models in recent years, achieving remarkable success in both forward and inverse problems [1, 2, 3, 4]. These include applications in additive manufacturing [5, 6], nuclear energy systems [7], and biomedical topics [8] to name a few. Physics-informed approaches [9, 10, 11] have also gained prominence, enabling the training process to dispense entirely, or in part, with labeled data pairs by relying instead on physical laws and residual minimization, akin to solving classical initial-boundary value problems of partial differential equations (PDEs). However, the way operator learning is employed differs fundamentally from traditional numerical methods for solving differential equations. Common approaches include full rollout (FR) models, which train on an entire spatiotemporal domain and then perform inference on that same domain [12, 13].

While the FR approach avoids treating time evolution explicitly, it often struggles with extrapolation beyond the training domain and fails to leverage the Markovian nature of many dynamical systems, where subsequent states inherently depend on previous ones. Alternatively, discrete autoregressive rollout (AR) methods have been introduced but face the limitations of training domain generalization and an additional susceptibility to error accumulation in time-dependent systems [14]. As a result, both approaches are ill-suited for making reliable long-term predictions akin to those obtained via classical simulations, limiting their utility as surrogate models.

Several recent efforts have sought to overcome these limitations by introducing architectural modifications in the NO to provide long-time prediction capabilities. For instance, in [15], an additional network was introduced to better capture temporal dependencies, while NO outputs were processed further by augmenting recurrent architectures to improve sequence modeling [16]. Other approaches introduce memory mechanisms [17, 18] to mitigate the non-Markovian behavior inherent in rollout-based methods. Nonetheless, these methods predominantly adopt generic time-series solutions without exploiting the rich dynamical information present in time-dependent systems.

The time-integration embedded operator learning framework introduced [19] addresses these limitations by leveraging the system's intrinsic dynamical structure, enabling near real-time inference, and shifting part of the computational load to an offline phase. This framework learns the discrete tangent from data and reuses it during inference through a numerical time integrator. Building on this foundation, we propose a significant advancement: a continuous temporal tangent space operator, which generalizes the notion of learned time evolution beyond discrete updates, transitioning the training process from a purely data-driven approach to a combination of physics-informed and data-driven methodologies. Additionally, we incorporate a residual prediction mechanism based on the current system state, which serves as an effective error predictor. This online residual tracking provides a means to assess prediction quality with minimal computational overhead, offering new opportunities for robust and efficient operator learning.

2 Methodology

2.1 Time-Integrator embedded Deep Operator Network

The Time-Integrator embedded Deep Operator Network (TI-DeepONet) framework [19] transforms the task of temporal prediction in dynamical systems into a derivative learning problem. Rather than predicting future states in an autoregressive manner, the model learns a discrete approximation of the system's temporal tangent space. Concretely, the current system state \mathbf{u}^n is passed through a DeepONet [1], which outputs the estimated temporal derivative $\hat{\mathbf{u}}_t^n$. This derivative is then integrated numerically via schemes like Euler or Runge-Kutta to yield the predicted next state $\hat{\mathbf{u}}^{n+1}$. The model is trained using a supervised loss computed between $\hat{\mathbf{u}}^{n+1}$ and the true state \mathbf{u}^{n+1} and learns an approximate tangent between the data pairs via the underlying scheme as a discrete operator. This setup tightly couples operator learning with time integration and provides a modular structure, where physical priors and numerical schemes can be systematically incorporated.

2.2 Physics-Informed Time-Integrated Deep Operator Network

In the following, we provide a comprehensive overview of how the physics-informed continuous tangent space operator is derived, along with a discussion on the training process, data sampling, and inference setup.

2.2.1 Network and Training Setup

To learn the temporal tangent (\mathbf{u}_t^n), we use a physics-informed DeepONet that performs the mapping $\mathcal{G} : \mathbf{u}^n \rightarrow \hat{\mathbf{u}}^n, \tilde{\mathbf{u}}_t^n$, where \mathbf{u}^n is the input field, $\hat{\mathbf{u}}^n$ is the reconstructed input field, and $\tilde{\mathbf{u}}_t^n$ is the predicted temporal tangent. For physics-informed training, we use automatic differentiation (AD) on $\hat{\mathbf{u}}^n$ to obtain the derivatives necessary to compute the loss terms: (1) PDE residual, \mathcal{L}_{PDE} , (2) initial condition (IC) loss, \mathcal{L}_{IC} , and (3) boundary condition

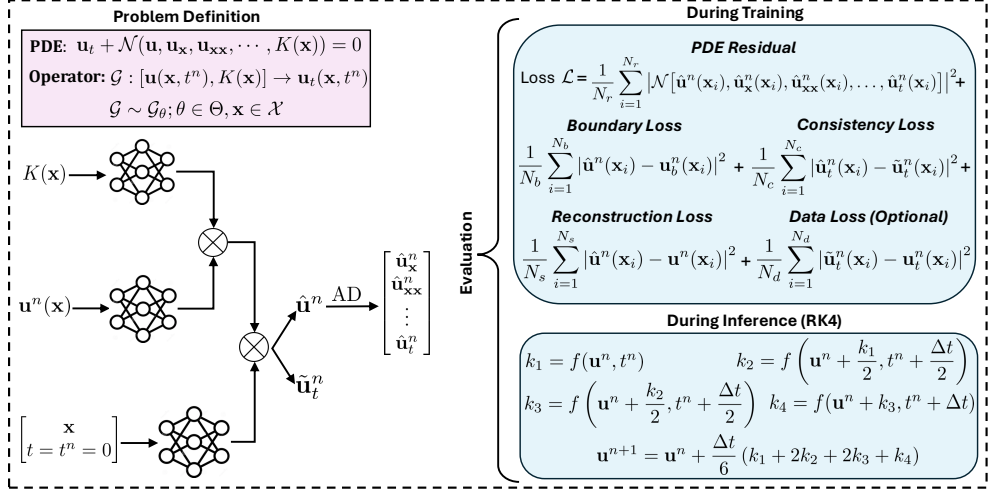


Figure 1: A schematic of the proposed physics-informed time-integrated deep operator network (PITI-DeepONet) architecture, which learns a continuous temporal tangent space operator that enables efficient and accurate time-stepping during inference.

(BC) loss, \mathcal{L}_{BC} . This part is identical to physics-informed training of any operator [10]. In addition, we introduce two new losses as follows. First, the discrepancy between \mathbf{u}^n and $\hat{\mathbf{u}}^n$ is quantified as reconstruction loss \mathcal{L}_R . Second, the consistency of the temporal derivative with the field is ensured using a consistency loss, \mathcal{L}_C , between the network-predicted derivative, $\tilde{\mathbf{u}}_t^n$, and the temporal derivative obtained via automatic differentiation (AD) on $\hat{\mathbf{u}}^n$, i.e., $\hat{\mathbf{u}}_t^n$. To accommodate the temporal dimension in this formulation, phantom values (e.g., zeros) are included as placeholders in the time input to the trunk network (to indicate the current time), alongside other coordinate inputs. Nonetheless, this still effectively reduces the dimensionality of the underlying problem to some extent as only a single value for the time domain has to be sampled. A schematic of the architecture described above is presented in Fig. 1. Moreover, as shown in the schematic, data-driven losses can be additionally imposed on the network outputs to achieve a hybrid setup. In total, this leads to 6 loss terms that are aggregated as the total loss. Note that all losses are computed as mean squared errors (MSE) and then combined with weighting factors $\lambda = \{\lambda_{PDE}, \lambda_R, \lambda_{BC}, \lambda_C, \lambda_u, \lambda_{u_t}\}$. The total loss reads $\mathcal{L} = \lambda_{PDE}\mathcal{L}_{PDE} + \lambda_R\mathcal{L}_R + \lambda_{BC}\mathcal{L}_{BC} + \lambda_C\mathcal{L}_C + \lambda_u\mathcal{L}_u + \lambda_{u_t}\mathcal{L}_{u_t}$, with the latter two being the data-driven losses, which are optional. Furthermore, the reconstruction loss and the data-driven loss for \mathbf{u}^n have the same formal structure, but are assigned different weights within the loss function to balance the influence of the data-driven and physics-informed terms. This allows for a purely physics-informed or a hybrid setup. All models are optimized using ADAM [20] with an exponential decay schedule for the learning rate. Note that there are other ways of formulating the physics-informed TI-DeepONet, but each have their disadvantages compared to the proposed method: i) one could discard the output, $\tilde{\mathbf{u}}_t^n$, and employ only AD to obtain the time derivative in inference. However, this would significantly increase the computational demand and reduce inference speed; ii) one could skip the consistency loss and directly incorporate the output, $\tilde{\mathbf{u}}_t^n$, in the PDE residual. However, as will be shown later in this work, the resulting network output is comparable or even inferior to our setup, so the more general formulation is preserved.

2.2.2 Sampling

Key to learning a temporal tangent space operator is to span the domain of solution states during inference with the limited samples used during training. Unlike other methods, which typically involve time evolution as seen in the traditional use of operators, this approach focuses solely on the time derivative of the current state. Consequently, a more meticulous sampling strategy is required. One potential remedy is to increase both the number and diversity of randomly sampled ICs to effectively span the relevant solution manifold. However, achieving sufficient coverage of the solution space through random sampling alone can be daunting—especially in the absence of domain knowledge to guide and reduce the training data requirements. In this work, we adopt a different strategy that leverages available domain knowledge in the form of solution samples \mathbf{u}^n and corresponding time derivatives \mathbf{u}_t^n at fixed time instances. These samples may originate from experiments, analytical solutions, numerical simulations, or even pre-trained surrogate models operating over longer time horizons. Once obtained, they are aggregated and used as inputs to the branch network, treated equivalently to IC samples. The trunk network, in turn, receives these inputs with phantom zeroes in the time dimension, omitting explicit time encoding, alongside spatial coordinates and any additional parameters.

2.2.3 Inference Setup

Having learned a continuous temporal tangent space operator, we can now exploit this for time-stepping-based inference. For each available state as branch input, the network predicts a replica (or reconstruction) of the input state as well as the corresponding temporal tangent (or time-derivative) of that state. To advance the solution in time, we utilize well-established, stable, and accurate time-stepping schemes commonly used for solving ordinary differential equations (ODEs). There are no constraints imposed on parameters such as model complexity, choice of numerical method, number of iterations, or time step size. To illustrate the flexibility of our approach, three representative numerical time integration schemes are considered.

First, the explicit Euler method is used, which is a first-order single-step scheme. Given \mathbf{u}^n at time step n and its time derivative $\tilde{\mathbf{u}}_t^n$ as obtained from the learned operator, the solution is advanced according to

$$\mathbf{u}^{n+1} = \mathbf{u}^n + \Delta t \tilde{\mathbf{u}}_t^n = \mathbf{u}^n + \Delta t \mathcal{G}_\theta(\mathbf{u}^n). \quad (1)$$

Second, the fourth-order Runge–Kutta method (RK4) is employed, representing a classical multi-stage scheme with improved accuracy through intermediate evaluations:

$$k_1 = \mathcal{G}_\theta(\mathbf{u}^n), \quad (2)$$

$$k_2 = \mathcal{G}_\theta \left(\mathbf{u}^n + \frac{\Delta t}{2} k_1 \right), \quad (3)$$

$$k_3 = \mathcal{G}_\theta \left(\mathbf{u}^n + \frac{\Delta t}{2} k_2 \right), \quad (4)$$

$$k_4 = \mathcal{G}_\theta \left(\mathbf{u}^n + \Delta t k_3 \right), \quad (5)$$

$$\mathbf{u}^{n+1} = \mathbf{u}^n + \frac{\Delta t}{6} (k_1 + 2k_2 + 2k_3 + k_4), \quad (6)$$

where k_1 , k_2 , k_3 , and k_4 are the intermediate RK4 slopes.

Third, the second-order Adams-Bashforth-Moulton method (ABM2) is included, functioning as a two-step predictor-corrector scheme that utilizes information from multiple time levels:

$$\text{Predictor: } \tilde{\mathbf{u}}^{n+1} = \mathbf{u}^n + \Delta t \left(\frac{3}{2} \mathcal{G}_\theta(\mathbf{u}^n) - \frac{1}{2} \mathcal{G}_\theta(\mathbf{u}^{n-1}) \right), \quad (7)$$

$$\text{Corrector: } \mathbf{u}^{n+1} = \mathbf{u}^n + \frac{\Delta t}{2} \left(\mathcal{G}_\theta(\mathbf{u}^n) + \mathcal{G}_\theta(\tilde{\mathbf{u}}^{n+1}) \right) \quad (8)$$

It should be noted that in the above numerical schemes employed during inference, \mathcal{G}_θ represents the learned operator, parametrized by θ , mapping the input state to its time derivative ($\tilde{\mathbf{u}}_t^n$). Only the time derivative output is used to perform numerical time integration. These integration schemes span a wide range of numerical properties in terms of stability, accuracy, and computational cost, making them suitable for evaluating the behavior of the proposed framework under varying conditions. We further distinguish between the training time step dt (used implicitly through sampled data) and the inference time step Δt (used explicitly during numerical integration), offering additional flexibility in evaluating generalization and stability behavior.

Another notable property of this method is the ability to monitor the residual, $\mathcal{R}(\mathbf{u}^n, \hat{\mathbf{u}}^n) = (\mathbf{u}^n - \hat{\mathbf{u}}^n)^2$, computed using the input state \mathbf{u}^n and the network prediction $\hat{\mathbf{u}}^n$. In theory, a well-learned state should correspond to a small residual, indicating consistency between the model's prediction and the governing dynamics. Conversely, a large residual may suggest that the current input lies outside the distribution of the training data, potentially leading to inaccurate predictions by the learned operator. This behavior effectively provides an intrinsic estimate of prediction quality, enabling a form of self-assessment within the inference process.

2.3 Reference Methods: Full Rollout and Autoregressive Rollout

To demonstrate the advantages of the proposed approach, we present a comprehensive comparison against state-of-the-art methods, including FR and AR. For FR, the operator is trained on the temporal domain, $t \in [0, 0.5]$ for all examples, learning to predict the entire spatiotemporal output field over this interval in a single shot (without respecting causality). In AR, the training process uses three temporal slices per trajectory, specifically at $t \in \{0, 0.25, 0.5\}$, to learn discrete mappings from each slice to the subsequent step. Within hybrid physics-informed and data-driven formulations, data losses for FR are applied continuously over the temporal domain, while in AR they are localized to the selected time slices with both being supplemented by physics-informed losses. The datasets used for data-driven and physics-informed terms are distinct but consistent across methods, ensuring a fair comparison. This design ensures a consistent and equitable comparison between FR and AR by providing both methods with access to identical training information. Note that the losses here are PDE, IC, BC, and a data loss, where IC refers to the reconstruction loss but is named IC to better reflect its purpose in numerical settings.

3 Numerical Results

Table 1: Minimum, mean, and maximum relative \mathcal{L}_2 error along with mean and standard deviation for 5 timed runs each over all test examples for three test cases in comparison of FR, AR, and time integration using explicit Euler, fourth-order Runge-Kutta (RK4), and second-order Adam-Bashforth-Moultons (ABM2) as inference scheme with $\Delta t = 0.01$. Irrespective of the inference scheme employed, PITI-DeepONet decreases the mean relative \mathcal{L}_2 errors by 84% (vs. FR) and 79% (vs. AR) for the one-dimensional heat equation; by 87% (vs. FR) and 98% (vs. AR) for the one-dimensional Burgers' equation; and by 42% (vs. FR) and 89% (vs. AR) for the two-dimensional Allen-Cahn equation. The timing includes residual calculation for PITI cases.

	Heat 1D @ $t = 5.0$		Burgers 1D @ $t = 1.0$		Allen-Cahn 2D @ $t = 1.0$	
	Min / Mean / Max	Inference in s	Min / Mean / Max	Inference in s	Min / Mean / Max	Inference in s
FR	0.82 / 1.5 / 24	1.4e-3 \pm 1.7e-5	0.048 / 0.13 / 0.56	5.8e-4 \pm 3.1e-5	0.13 / 0.20 / 0.28	9.5e-4 \pm 1.7e-5
AR	0.11 / 1.2 / 23	6.8e-2 \pm 3.9e-5	0.15 / 0.94 / 11	1.6e-3 \pm 7.6e-5	0.49 / 1.1 / 1.7	9.2e-3 \pm 2.2e-4
PITI (Euler)	0.029 / 0.24 / 3.4	7.5e-2 \pm 1.7e-5	0.0084 / 0.018 / 0.26	1.4e-2 \pm 9.0e-5	0.079 / 0.12 / 0.16	8.9e-3 \pm 3.1e-5
PITI (RK4)	0.029 / 0.24 / 3.3	2.0e-1 \pm 2.6e-4	0.0038 / 0.017 / 0.26	3.8e-2 \pm 8.5e-5	0.079 / 0.12 / 0.16	2.6e-2 \pm 3.7e-5
PITI (ABM2)	0.029 / 0.24 / 3.3	1.7e-2 \pm 2.2e-4	0.0039 / 0.017 / 0.26	3.2e-2 \pm 3.6e-5	0.079 / 0.12 / 0.16	2.4e-3 \pm 6.1e-5

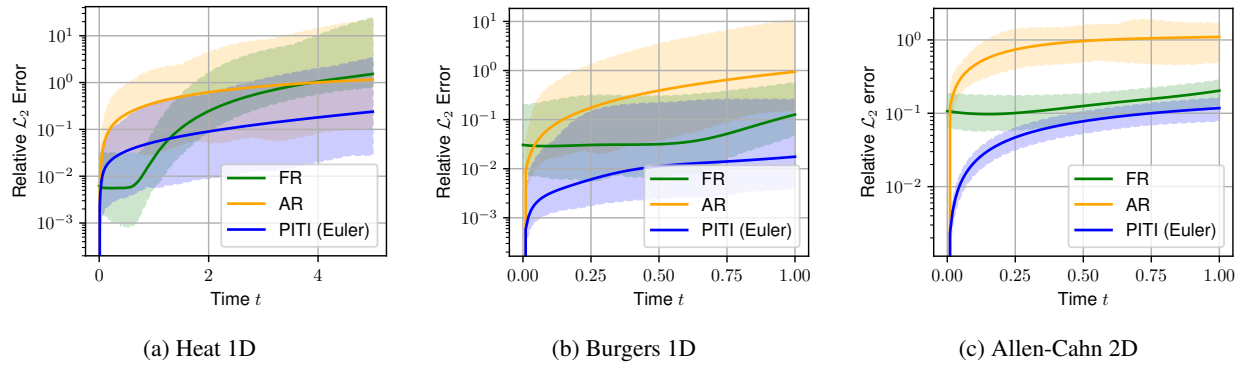


Figure 2: Relative \mathcal{L}_2 error over time for the three PDEs in comparison of FR, AR, and time integration using explicit Euler with $\Delta t = 0.01$. Depicted are the mean as well as minimum and maximum value for all test examples. Only inference with explicit Euler is depicted, but all methods show similar values in inference also as shown in Tab. 1.

The subsequent sections detail the setup and results for the three examples of Heat and Burgers' equations in one dimension and Allen-Cahn equation in two dimensions. Fig. 2 and Tab. 1 present a short overview of the performance of our proposed method compared to FR and AR. The relative \mathcal{L}_2 error = $\|\hat{\mathbf{u}}^n - \mathbf{u}^n\|_2 / \|\mathbf{u}^n\|_2$ was employed on the predicted field as standard metric for comparison with the field, depicting relative deviation from the ground truth. Furthermore, all hyperparameters were optimized using *optuna* [21]. Metric for AR and FR models was to reduce the relative \mathcal{L}_2 error on the complete validation data for the field output, while PITI models were optimized on the relative \mathcal{L}_2 error of the time derivative within the complete validation data. Optimization was performed on a discrete set of pre-chosen options to ease interpretation. At least 20 runs with a minimum of 6h run time were performed per setup. This included depth and width of branch and trunk nets, hidden dimension, training epochs, learning rate settings, loss weights, as well as information on how to obtain multiple outputs by splitting either or both trunk and branch outputs where necessary. For networks with CNNs in the branch, the number of layers, kernels per layer, depth and size of the dense layers, if pooling was applied and if so whether average or max pooling, as well as dense and CNN activation. Stride for convolutions and pooling as well as kernel size for convolutions were fixed to 2 in each dimension. Interestingly, all CNNs converged to the same structure including activation functions except for width of the dense layer. The results are given in Tab. 2 for everything except loss weights which are presented in Tab. 3. Random seed choice in physics-informed scientific machine learning can influence solution diversity and optimization outcomes, especially in problems with multiple valid solutions, since random initialization may lead to discovering different solutions [22]. However, as the obtained results showed good agreement during training with the used input, a single random seed per numerical examples was utilized. This is a standard, resource-efficient practice within the field, but we acknowledge that additional seeds might yield alternative results in non-convex or multi-solution settings. Training and inference were performed on an *NVIDIA A40* GPU with 48 GB of memory, utilizing CUDA version 12.4 and NVIDIA driver version 550.54.15, with the GPU operating in a Linux environment running the 64-bit Debian-based GNU/Linux operating system under kernel version 6.1.0-34-cloud-amd64. The framework was built in *Python*

3.11.2 based on *JAX* [23] and *Flax* [24] with integration of tools from the *DeepMind Ecosystem* [25]. The full code included utilized package versions will be available at <https://github.com/lmandl/PITI-DeepONet> upon publication of this work. The dataset for the underlying cases was generated from scratch for this paper. While some datasets exists and either the data or the code to generate the dataset are publicly available (cf. [10] for Burger's equation), so far no dataset includes high-accuracy time derivatives. Hence, the need for this data to track accuracy of our method or additional input for hybrid data-driven and physics-informed approaches, required generation of new datasets that fit the purpose of solving PDEs.

Table 2: Hyperparameter values after optuna optimization for all setups. Branch inputs are 128 sensors for the heat equation, 101 sensors for Burgers' equation, and (16, 16) for the Allen-Cahn equation. Trunk input dimensions are 2 for the heat and Burgers' equation (t, x) and 3 for the Allen-Cahn equation (t, x, y). For models with the special form for time-evolution PDEs, the trunk input is reduced by the time dimension. p denotes latent dimension for the branch and trunk nets. All models are unstacked DeepONet that are optimized with Adam optimizer and exponential learning rate decay. *Hy.* indicates a hybrid data-driven and physics-informed model, while *spec.* indicates the special form. The architecture of the convolutional neural network (CNN) used for all three Allen-Cahn (AC) cases consists of an initial 2D convolution (Conv) with a stride of 2 and 2 filters, followed by average pooling (AvgPool) with a stride of 2, then another 2D convolution with a stride of 2 and 4 filters, and another average pooling with a stride of 2. The output is then flattened and passed through a dense layer, with the size specified in the column for the branch network. Activation function for all models including the CNNs is hyperbolic tangent. Timing is averaged over the whole training including 100 validation evaluations equally distributed throughout training.

Model	branch	trunk	p	epochs	exp. lr decay			split		IT/s	
					base	rate	steps	branch	trunk		
Heat	PITI	8x[128]	10x[128]	256	300,000	1e-4	0.9	40,000	False	True	151.76
	FR	8x[64]	8x[32]	64	300,000	5e-4	0.85	50,000	False	False	150.95
	AR	4x[256]	10x[256]	64	300,000	5e-5	0.95	10,000	False	False	171.08
	PITI <i>spec.</i>	8x[128]	8x[256]	128	300,000	5e-5	0.8	100,000	False	True	309.59
Burgers	PITI	10x[256]	8x[64]	64	500,000	1e-4	0.9	100,000	False	True	206.33
	PITI <i>Hy.</i>	8x[128]	8x[128]	128	300,000	1e-4	0.95	5,000	True	True	395.96
	AR <i>Hy.</i>	6x[256]	10x[256]	256	200,000	5e-5	0.9	10,000	False	False	338.76
	FR <i>Hy.</i>	8x[128]	6x[64]	256	100,000	1e-3	0.85	7,500	False	False	168.23
	PITI <i>spec.</i>	6x[64]	10x[32]	128	200,000	5e-5	0.8	20,000	True	False	625.04
AC	PITI <i>Hy.</i>	CNN*, [256]	6x[32]	128	50,000	1e-3	0.9	100,000	False	True	129.88
	AR <i>Hy.</i>	CNN*, [64]	6x[128]	256	100,000	1e-3	0.95	7,500	False	False	192.64
	FR <i>Hy.</i>	CNN*, [64]	6x[128]	128	25,000	1e-4	0.95	40,000	False	False	22.14

* CNN consists of Conv2D[2], AvgPool, Conv2D[4], AvgPool, where Conv2D[j] indicates j filters in that layer

Table 3: Loss weights after optuna optimization for all setups. Factors for reconstruction loss in time integration and initial condition loss in rollout settings are combined into one column as they essentially have the same significance.

Model	Loss Weights						
	λ_{PDE}	λ_R	λ_{BC}	λ_u	λ_{u_t}	λ_C	
Heat	PITI	1	10	1	-	-	1
	FR	1	2.5	1	-	-	-
	AR	10	100	1	-	-	-
	PITI <i>spec.</i>	10	20	1	-	-	-
Burgers	PITI	2	10	1	-	-	4
	PITI <i>Hy.</i>	1	1	20	2	50	20
	AR <i>Hy.</i>	5	10	1	25	-	-
	FR <i>Hy.</i>	25	100	10	1	-	-
	PITI <i>spec.</i>	2	20	1	10	20	-
AC	PITI <i>Hy.</i>	2.5	2.5	1	5	25	10
	AR <i>Hy.</i>	10	1	2	10	-	-
	FR <i>Hy.</i>	10	50	1	10	-	-

3.1 One-dimensional Heat Equation

As an introductory example, we present the 1D heat equation with the form:

$$\frac{\partial T}{\partial t} = 0.01 \frac{\partial^2 T}{\partial x^2}, \quad (t, x) \in [0, \infty) \times [0, 1] \quad (9)$$

with Dirichlet BC $T(t, 0) = T(t, 1) = 0$. IC, $T(0, x) = f(x)$, is sampled from a periodic Gaussian process with $f(0) = f(1) = 0$, length scale = 0.1, and variance $\sigma^2 = 10,000$. The spatial domain was discretized using 128 grid points. The training was performed with a purely physics-informed setup using 4,800 input profiles sampled from 1,600 ICs at the time steps $t = \{0, 0.25, 0.5\}$. Note our remarks in the section on sampling (Sec. 2.2.2), as this does not change the underlying problem but rather represents a method for sampling the required profiles to cover the domain. The discrete time step for AR is set to $dt = 0.01$, while FR training was performed on $t \in [0, 0.5]$ with the same timestep. Additionally, 400 validation samples on $t \in [0, 1]$ and 500 test samples on $t \in [0, 5]$, both with time step $dt = 0.01$ were used.

The dataset is generated by solving Eq. 9 with Dirichlet BCs on the mentioned spatiotemporal domain. A uniform grid with $N_x = 128$ points is used for space, and the solution is computed over $N_{t, \text{fine}} = 10,000$ fine time steps with a step size Δt_{fine} , which inherently satisfies the stability requirements of the numerical scheme. The IC $u_0(x)$ is sampled from a periodic Gaussian random field. The numerical solution is obtained using an explicit finite-difference scheme, with second-order accurate spatial derivatives in the interior and fourth-order one-sided differences at the boundaries. The time derivative $\partial_t u$ is computed at each step, and BCs are enforced by setting $u(t, 0) = u(t, 1) = 0$. The solution is then downsampled to a coarse temporal grid with $N_t = 100$ intervals using linear interpolation, yielding the coarse fields $u(t, x)$ and $\partial_t u(t, x)$. The dataset includes $N_{\text{train}} = 2,000$ samples for training and $N_{\text{test}} = 500$ for testing, with solutions recorded for $T = 1$ and $T_{\text{test}} = 5$, respectively.

Final mean relative \mathcal{L}_2 errors observed were 6.81e-2 on the training set and 8.20e-2 on the validation set for the time derivative using TI, whereas for the field values, AR achieved 4.09e-3 and 2.04e-3, and FR achieved 6.63e-3 and 7.20e-3 on the training and test sets, respectively (see Fig. 4 for full trajectories). Although FR and AR achieve an order of magnitude better results on the training domain $t \in [0, 1]$, if used in inference, PITI beats AR on $t \in [0, 1]$ and both AR and FR on $t \in [0, 5]$ as shown in Fig. 2a and Tab. 1 with full field plots and differences for a single test example for PITI using explicit Euler, AR, and FR in Fig. 7. Furthermore, all employed time integration methods show near identical results as per Tab. 1 as well as Fig. 6 which depicts behavior over time including residuals. Fig. 3 illustrates inference using explicit Euler, alongside the squared difference between the reference and prediction, as well as the calculated residual on the network's output. As hypothesized, the squared difference and the residual exhibit similar patterns, highlighting the potential of using the residual as an indicator of prediction quality. This relationship becomes even more pronounced when computing the mean absolute error (MAE) and the Pearson correlation coefficient ρ over all test examples, yielding a MAE of 2.04e-3 and $\rho = 0.997$, thereby indicating an almost perfect correlation across the dataset.

As mentioned in Section 2.2.1, a special formulation can be employed for time-evolution PDEs, such as the heat equation, where the time derivative appears in isolation and all other terms can be moved to the right-hand side. This alternative setup demonstrates comparable performance to the standard (vanilla) formulation, with mean relative \mathcal{L}_2 errors of 2.39e-1 for the standard and 2.48e-1 for the special formulation (Fig. 5).

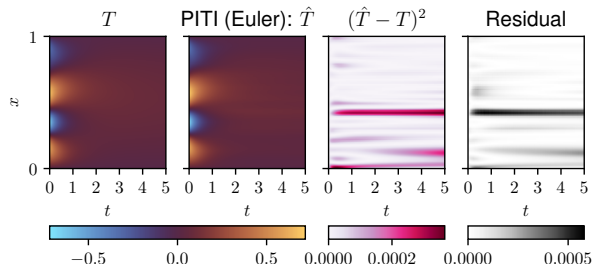


Figure 3: 1D Heat equation (Mean rel. \mathcal{L}_2 error 7.60e-2): Comparison of reference data and PITI-DeepONet with explicit Euler alongside the squared difference of the computed field and the residuals during inference. Mean absolute error between squared difference and predicted residual for this example is 3.72e-5 and Pearson's correlation coefficient is $\rho = 0.9985$.

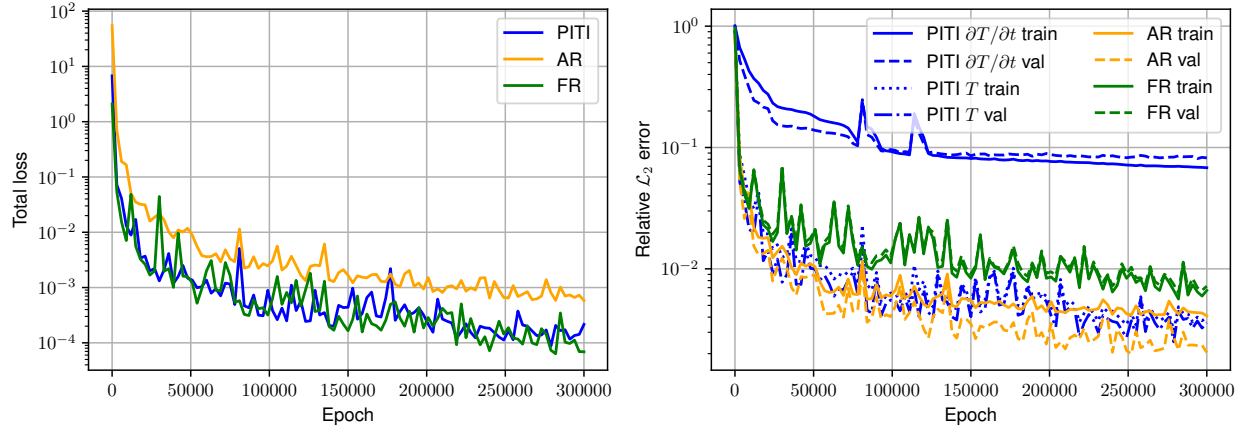


Figure 4: 1D Heat equation: Total loss during training alongside mean relative \mathcal{L}_2 error on the train and validation set for full rollout (FR), autoregressive (AR), and time integration (PITI) model. The relative \mathcal{L}_2 error on both network outputs is provided for the PITI model. Hyperparameters were adapted per model as per table 2.

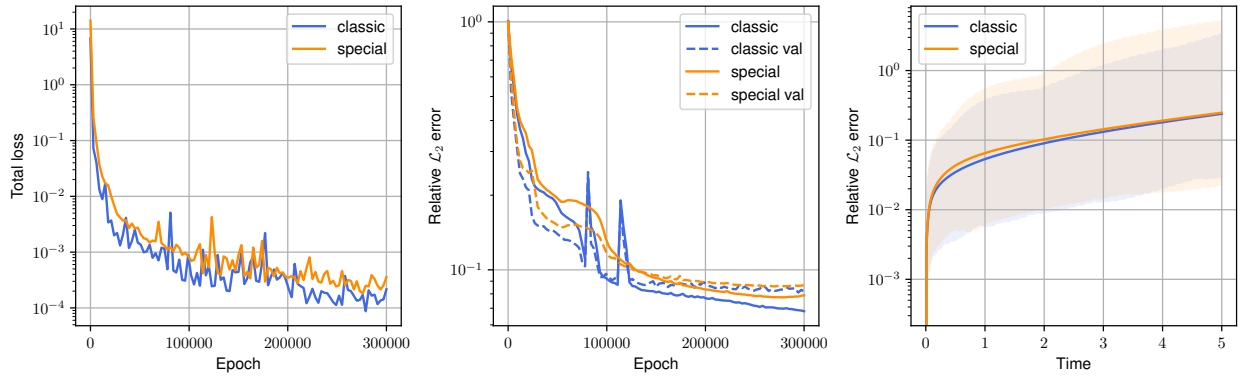


Figure 5: 1D Heat equation: Comparison of time integration models in the vanilla form and special form for time-evolution partial differential equations including total loss and mean relative \mathcal{L}_2 error on train and validation set during training. Only the relative \mathcal{L}_2 error on the time derivative is provided here. The right plot shows the performance during inference with the fully trained model using an explicit Euler scheme while depicting minimum, mean, and maximum value of the relative \mathcal{L}_2 error per time step.

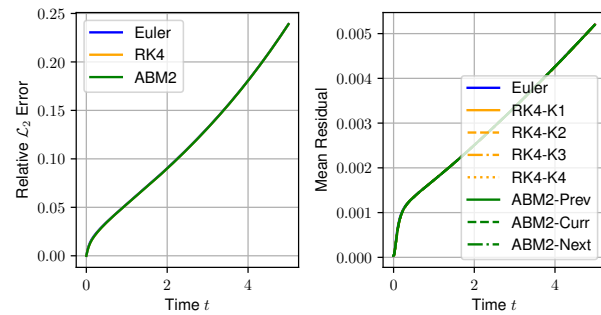


Figure 6: 1D Heat equation: Comparison of different time integration (PITI) methods using explicit Euler, fourth-order Runge-Kutta (RK4) and second-order Adam-Bashforth-Moultons (ABM2) with mean relative \mathcal{L}_2 error on the left and predicted residuals on the right over all test examples.

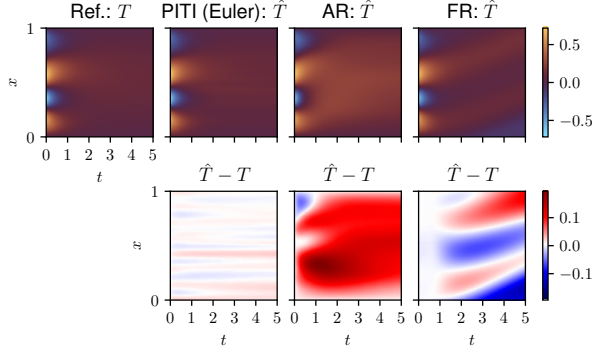


Figure 7: 1D Heat equation: Comparison of predictions made using time integration (PITI) with explicit Euler, autoregressive and full rollout alongside the differences for each method.

3.2 One-dimensional Burgers' Equation

After examining heat conduction, the Burgers' equation is introduced as the next example, highlighting the transition from diffusion-dominated to hyperbolic dynamics, incorporating nonlinear advection and viscosity effects in fluid flow. The equation reads as:

$$\frac{\partial u}{\partial t} = 0.01 \frac{\partial^2 u}{\partial x^2} - u \frac{\partial u}{\partial x}, \quad (t, x) \in [0, \infty) \times [0, 1] \quad (10)$$

with periodic BCs $u(t, 0) = u(t, 1)$ and $\frac{\partial u}{\partial x}(t, 0) = \frac{\partial u}{\partial x}(t, 1)$. The IC $u(0, x) = f(x)$ was sampled from a Gaussian process with spectral density $S(k) = \sigma^2(\tau^2 + (2\pi k)^2)^{-\gamma}$, $\sigma = 25$, $\tau = 5$, $\gamma = 4$, periodic on $x \in [0, 1]$. Equivalently, the covariance kernel is $K(\mathbf{x}, \mathbf{x}') = \int_{-\infty}^{\infty} S(k) e^{2\pi i k (\mathbf{x} - \mathbf{x}')} dk$. A spatial resolution of 101 grid points was used.

The dataset is generated by solving Eq. 10 on a periodic spatial domain $x \in [0, 1]$. The spatial domain is discretized using $s = 4,096$ grid points, while outputs are captured at $n_{\text{steps}} + 1 = 101$ evenly spaced time steps over $t \in [0, 1]$. The ICs $u_0(x)$ are sampled from stationary Gaussian random fields (GRFs) with covariance kernel $C = \sigma^2(-\Delta + \tau^2 I)^{-\gamma}$. For GRF generation, the Fourier coefficients are drawn from $\mathcal{N}(0, \sigma^2)$ and scaled appropriately to enforce the specified covariance structure, yielding smooth, periodic initial profiles. The Burgers' equation is advanced in time using an operator-splitting spectral method implemented with the `spin` function from Chebfun [26], which combines linear evolution via viscosity νu_{xx} with nonlinear convection $-uu_x$. The solution $u(t, x)$ is represented as a Chebyshev interpolant at each time step and stored. The corresponding time derivative $\partial_t u(t, x)$ is independently computed at each output time by substituting the solution into the original Burgers' equation. Consistency checks are performed to ensure the accuracy of $\partial_t u(t, x)$ using both finite differences and the governing PDE. The dataset consists of $N = 2,500$ realizations of $u_0(x)$, where each realization evolves under the Burgers' dynamics and is evaluated on a reduced grid of $n = 101$ spatial points.

In this case, we utilize the hybrid setup by considering 1,200 IC profiles sampled at $t = 0$ for purely physics-informed training (TI at $t = 0$, AR with $dt = 0.01$, FR on $t \in [0, 0.5]$) and additionally 1,200 profiles sampled from 400 trajectories at $t = \{0, 0.25, 0.5\}$ used for both physics-informed and data-driven training. Once again, this data could also be sampled randomly with consistency of u and $\frac{\partial u}{\partial t}$, but sampling from trajectories ameliorates the sampling. The data-driven losses were evaluated for PITI using $\frac{\partial u}{\partial t}$ at $t = 0$ by flattening, AR uses u at $t = 0$, $dt = 0.01$ by using the sampled and next step, and FR uses u at $t = \{0, 0.25, 0.5\}$. Final mean relative \mathcal{L}_2 error was 4.41e-2 on the train and 7.56e-2 on the validation set for the time derivative using TI, whereas AR was 1.50e-2 and 3.02e-2, and FR was 6.16e-2 and 5.44e-2 on the field directly (See Fig. 11 for full trajectories). As the values are now in the same range, with a slight advantage for AR, it comes as no surprise that PITI clearly yields the best results, as shown in Fig. 2b and Tab. 1. Explicit Euler provides slightly worse results compared to RK4 and ABM2 during inference with PITI models (Fig. 9 for full trajectories). Fig. 8 illustrates the difficulty of AR and FR in accurately capturing the shock formation. A further study is presented in Fig. 10 showing inference with different timesteps, achieving mean relative \mathcal{L}_2 error at the end of testing domain of 1.69e-2 for $\Delta t = 0.001$, 1.75e-2 for $\Delta t = 0.01$, and 4.86e-2 for $\Delta t = 0.1$, where the first satisfies the CFL condition. This becomes evident as the largest time step fails to capture the full dynamics, while the middle time step, despite exceeding the CFL condition, still exhibits stable performance.

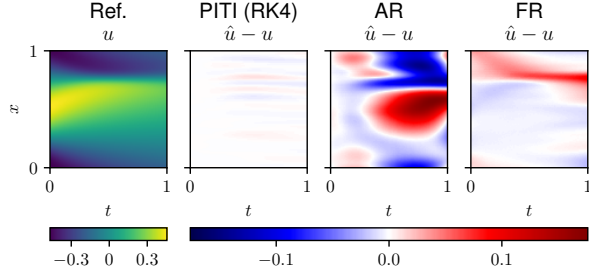


Figure 8: 1D Burgers' equation: Reference and difference of predictions to reference using time integration with fourth-order Runge-Kutta, autoregressive and full rollout.

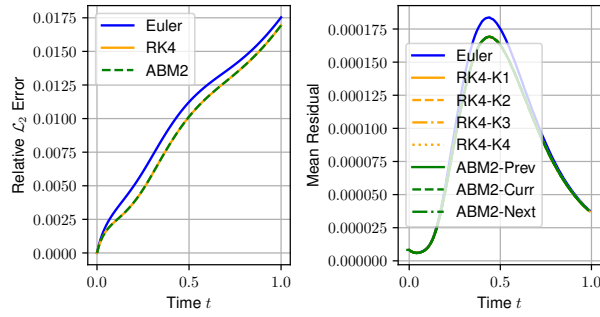


Figure 9: 1D Burgers' equation: Comparison of different time integration (PITI) methods using explicit Euler, fourth-order Runge-Kutta (RK4) and second-order Adam-Bashforth-Moulton (ABM2) with mean relative \mathcal{L}_2 error on the left and predicted residuals on the right over all test examples.

The full trajectories as well as the residuals obtained during inference are shown in Fig. 13, with full field plots available in the Fig. 10. The residuals for different time steps (Fig. 13) as well as different methods (Fig. 9) indicate a regime around the middle of the testing domain that was learned less accurately compared to states before and after. This is discernible due to an increase in the mean residual over all test examples, followed by a reduction back to smaller residual values. One could exploit this to adaptively resample profiles from this region of increased residuals in order to reduce the overall error. The MAE between the squared difference and residual for explicit Euler with $\Delta t = 0.01$ is $2.63\text{e-}5$ with Pearson's correlation coefficient $\rho = 0.9996$, once again suggesting that this correlation can be leveraged to obtain higher quality predictions. The last study for this example includes the already displayed classic form in a hybrid setting against the special form for time-evolution PDEs (mean relative \mathcal{L}_2 error = $3.62\text{e-}2$) alongside the classic form without additional data (mean relative \mathcal{L}_2 error $2.07\text{e-}1$). Thus, the chosen setup outperforms the data-free setting by more than an order of magnitude while still halving the error compared to the special case, thus indicating better performance on more complex equations.

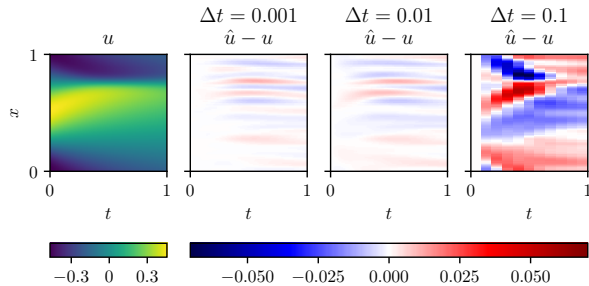


Figure 10: 1D Burgers' equation: Reference and difference of predictions to reference using time integration with explicit Euler and different time steps.

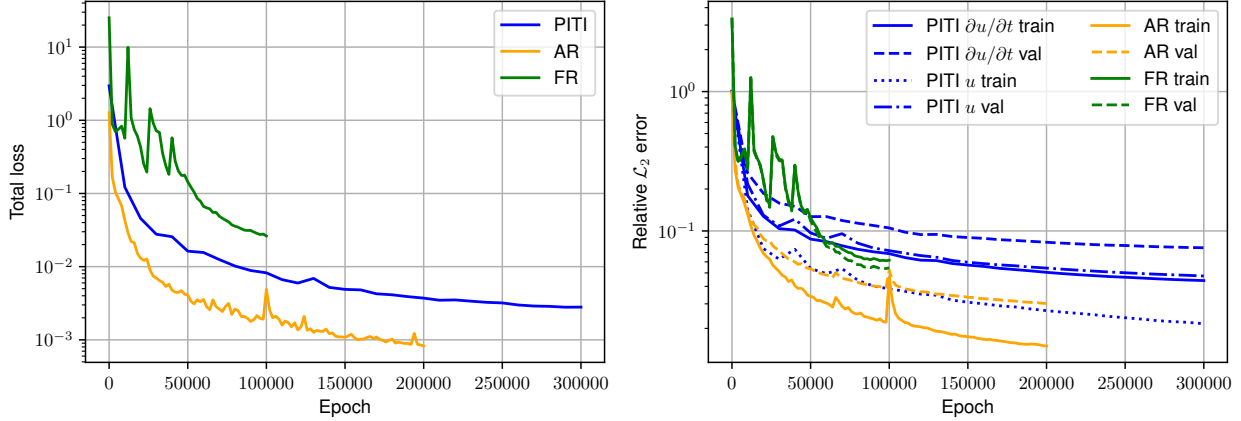


Figure 11: 1D Burgers' equation: Total loss during training alongside mean relative \mathcal{L}_2 error on the train and validation set for full rollout (FR), autoregressive (AR), and time integration (PITI) model. The relative \mathcal{L}_2 error on both network outputs is provided for the PITI model. Hyperparameters were adapted per model as per table 2.

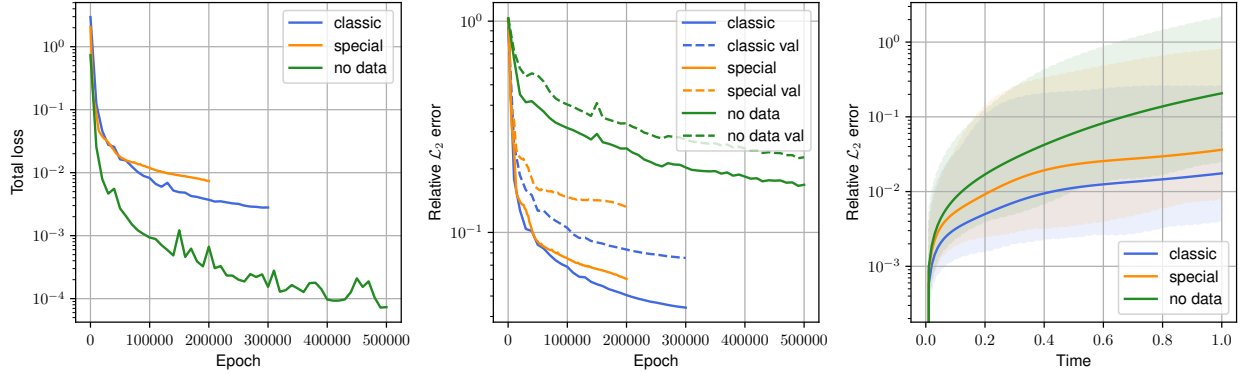


Figure 12: 1D Burgers' equation: Comparison of time integration models in the vanilla form and special form for time-evolution partial differential equations alongside a purely physics-informed training including total loss and mean relative \mathcal{L}_2 error on train and validation set during training. Only the relative \mathcal{L}_2 error on the time derivative is provided here. The right plot shows the performance during inference with the fully trained model using an explicit Euler scheme while depicting minimum, mean, and maximum value of the relative \mathcal{L}_2 error per time step.

3.3 Two-dimensional Allen-Cahn Equation

The final example we consider is the two-dimensional Allen–Cahn equation, governed by:

$$\frac{\partial u}{\partial t} = 0.05^2 \left(\frac{\partial^2 u}{\partial x^2} + \frac{\partial^2 u}{\partial y^2} \right) - (u^3 - u) \quad (11)$$

for $(t, x, y) \in [0, \infty) \times [0, 1] \times [0, 1]$ with periodic BCs $u(t, 0, y) = u(t, 1, y)$ and $u(t, x, 0) = u(t, x, 1)$. This PDE is used to investigate phase–field dynamics on a 16×16 spatial grid. The IC $u(0, x, y) = f(x, y)$ was sampled from a smooth periodic Gaussian random field (correlation length = 0.1) with linear mapping to $f(x, y) \in [-1, 1]$.

The dataset is generated by solving Eq. 11 on the periodic spatial domain discretized using a uniform 16×16 grid. The temporal evolution is computed up to a final time $T_{\text{final}} = 5.0$ using an exponential time-differencing fourth-order Runge–Kutta (ETDRK4) scheme. The coarse time step $\Delta t = 0.01$ is subdivided into 200 finer steps, resulting in a fine time resolution $\Delta t_{\text{fine}} = \Delta t / 200$. For spatial discretization, the Laplace operator is represented in spectral space using wavenumbers derived from a Fourier transform grid. Initial conditions are sampled from Gaussian-filtered random fields, smoothed by a low-pass filter, and mapped to the range $[-1, 1]$. During the simulation, the solution $u(t, x, y)$ and its time derivative $\partial_t u(t, x, y)$ are recorded on a coarse temporal grid spanning $n_{\text{coarse}} = T_{\text{final}} / \Delta t + 1$ snapshots. Additionally, the real-space energy functional $E = \int \left(\frac{\varepsilon^2}{2} |\nabla u|^2 + \frac{1}{4} (u^2 - 1)^2 \right) dx dy$ is computed at each snapshot

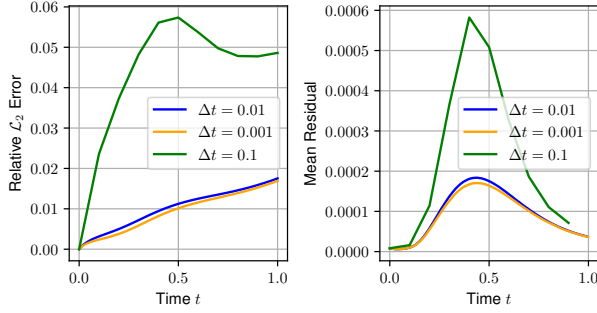


Figure 13: 1D Burgers’ equation: Comparison of explicit Euler as time integration (TI) method with different time steps (Δt) during inference. Mean relative \mathcal{L}_2 error is shown on the left and predicted residuals on the right over all test examples.

to monitor consistency and stability. The dataset consists of $N_{\text{train}} = 2,000$ training samples and $N_{\text{test}} = 500$ test samples, with unique ICs for each sample.

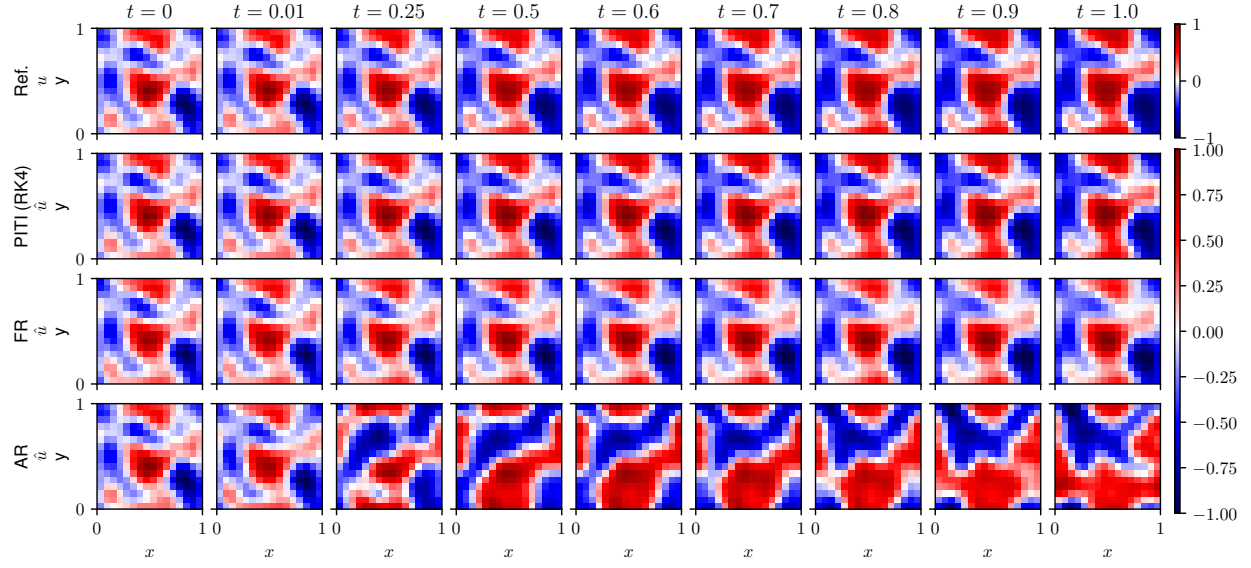
The same hybrid setup employed in the 1D Burgers’ case is utilized here: 400 validation and 500 test samples on $t \in [0, 1]$ with $dt = 0.01$, 1,200 profiles at $t = 0$ for physics-informed training, and 1,200 data points sampled from 400 trajectories at $t = \{0, 0.25, 0.5\}$. The branch network for this setup was a convolutional neural network (details in Tab. 2). The final mean relative \mathcal{L}_2 error for the time derivative using PITI was $4.43\text{e-}1$ on the training set and $3.64\text{e-}2$ on the validation set, whereas AR yielded $1.28\text{e-}1$ and $1.12\text{e-}1$, and FR incurred $1.44\text{e-}1$ and $1.45\text{e-}1$ on the field directly (see Fig. 15 for full trajectories). Once again, although PITI exhibits a higher error on the traced time derivative metric compared to the error on the field itself, it significantly outperforms AR and FR, as shown in Tab. 1 and Fig. 2c, where the upper limit for PITI using RK4 consistently surpasses the mean performance of other methods.

Furthermore, the chosen time integration scheme during inference has negligible influence on the errors (Tab. 1 and Fig. 16). An example including error comparison for the methods is shown in Fig. 14b, demonstrating the struggle of AR to capture the dynamics even within the training domain, and FR starting to slightly diverge in extrapolation with relatively low dynamics in the remaining field. In contrast, PITI exhibits comparably more gradual divergence, yet its residual continues to grow in the later states, thus hinting at the potential to improve sampling of states to sufficiently represent the underlying dynamics (Fig. 16). Once again, residual and squared difference exhibit near perfect correlation, with a MAE of $1.84\text{e-}3$ and Pearson’s correlation coefficient $\rho = 0.997$ for explicit Euler with $\Delta t = 0.01$.

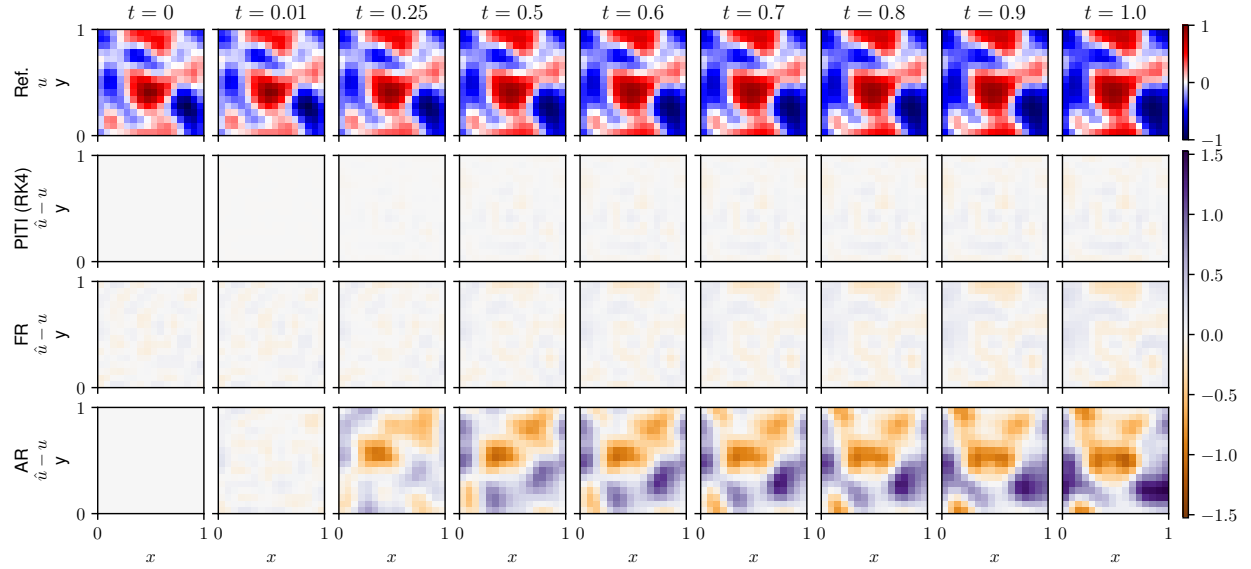
3.4 Ablation Studies

Table 4: Seed sensitivity analysis for the final model configurations. Each method (PITI, AR, FR) was trained with five different random seeds. For each run, the relative \mathcal{L}_2 error was computed over all test samples and summarized by its mean, minimum, and maximum at two time points corresponding to the end of the training domain and the end of the testing domain for each problem (Heat 1D: $t = 0.5$ and $t = 5.0$; Burgers 1D: $t = 0.5$ and $t = 1.0$; Allen-Cahn 2D: $t = 0.5$ and $t = 1.0$). Table entries report the overall mean and between-seed standard deviation across the five runs, formatted as $\mu \pm \sigma$.

		Heat 1D		Burgers 1D		Allen-Cahn 2D	
		$t = 0.5$	$t = 5.0$	$t = 0.5$	$t = 1.0$	$t = 0.5$	$t = 1.0$
Mean	PITI	$3.5\text{e-}2 \pm 3.9\text{e-}3$	$2.2\text{e-}1 \pm 3.4\text{e-}2$	$1.1\text{e-}2 \pm 6.2\text{e-}4$	$1.8\text{e-}2 \pm 1.8\text{e-}3$	$7.9\text{e-}2 \pm 1.4\text{e-}3$	$1.2\text{e-}1 \pm 2.6\text{e-}3$
	AR	$2.2\text{e-}1 \pm 3.3\text{e-}2$	$1.5\text{e-}0 \pm 5.4\text{e-}1$	$2.4\text{e-}1 \pm 8.7\text{e-}2$	$6.0\text{e-}1 \pm 2.1\text{e-}1$	$9.9\text{e-}1 \pm 7.2\text{e-}2$	$1.1\text{e}0 \pm 7.0\text{e-}2$
	FR	$5.7\text{e-}3 \pm 3.2\text{e-}4$	$1.3\text{e}0 \pm 1.4\text{e-}1$	$3.5\text{e-}2 \pm 2.0\text{e-}3$	$1.2\text{e-}1 \pm 2.1\text{e-}2$	$1.3\text{e-}1 \pm 2.3\text{e-}2$	$2.1\text{e-}1 \pm 1.8\text{e-}2$
Min	PITI	$3.8\text{e-}3 \pm 4.2\text{e-}4$	$2.8\text{e-}2 \pm 1.7\text{e-}3$	$2.5\text{e-}3 \pm 3.9\text{e-}4$	$4.4\text{e-}3 \pm 5.9\text{e-}4$	$5.3\text{e-}2 \pm 1.5\text{e-}3$	$7.7\text{e-}2 \pm 3.6\text{e-}3$
	AR	$3.2\text{e-}2 \pm 8.3\text{e-}3$	$1.3\text{e-}1 \pm 5.9\text{e-}2$	$4.1\text{e-}2 \pm 7.0\text{e-}3$	$1.0\text{e-}1 \pm 3.3\text{e-}2$	$1.8\text{e-}1 \pm 3.6\text{e-}2$	$1.9\text{e-}1 \pm 4.3\text{e-}2$
	FR	$1.4\text{e-}3 \pm 3.4\text{e-}4$	$6.3\text{e-}1 \pm 1.3\text{e-}1$	$7.0\text{e-}3 \pm 7.2\text{e-}4$	$3.9\text{e-}2 \pm 1.0\text{e-}2$	$4.0\text{e-}2 \pm 7.1\text{e-}3$	$7.1\text{e-}2 \pm 1.3\text{e-}2$
Max	PITI	$1.7\text{e-}1 \pm 3.4\text{e-}2$	$2.5\text{e-}0 \pm 6.6\text{e-}1$	$1.9\text{e-}1 \pm 3.7\text{e-}2$	$2.5\text{e-}1 \pm 7.1\text{e-}2$	$1.1\text{e-}1 \pm 6.0\text{e-}3$	$1.8\text{e-}1 \pm 1.2\text{e-}2$
	AR	$9.7\text{e-}1 \pm 2.1\text{e-}1$	$3.2\text{e}1 \pm 1.7\text{e}1$	$1.8\text{e}0 \pm 1.0\text{e}0$	$5.2\text{e}0 \pm 3.5\text{e}0$	$3.3\text{e}0 \pm 4.1\text{e-}1$	$2.9\text{e}0 \pm 3.8\text{e-}1$
	FR	$2.9\text{e-}2 \pm 5.9\text{e-}3$	$2.1\text{e}1 \pm 2.5\text{e}0$	$2.5\text{e-}1 \pm 3.7\text{e-}2$	$5.3\text{e-}1 \pm 9.3\text{e-}2$	$3.4\text{e-}1 \pm 6.8\text{e-}2$	$4.7\text{e-}1 \pm 6.6\text{e-}2$



(a) Reference and predictions



(b) Reference and absolute error in predictions with respect to reference

Figure 14: 2D Allen-Cahn equation: Reference, predictions, and absolute error in predictions with respect to reference using time integration with fourth-order Runge-Kutta (RK4), autoregressive and full rollout at different time points.

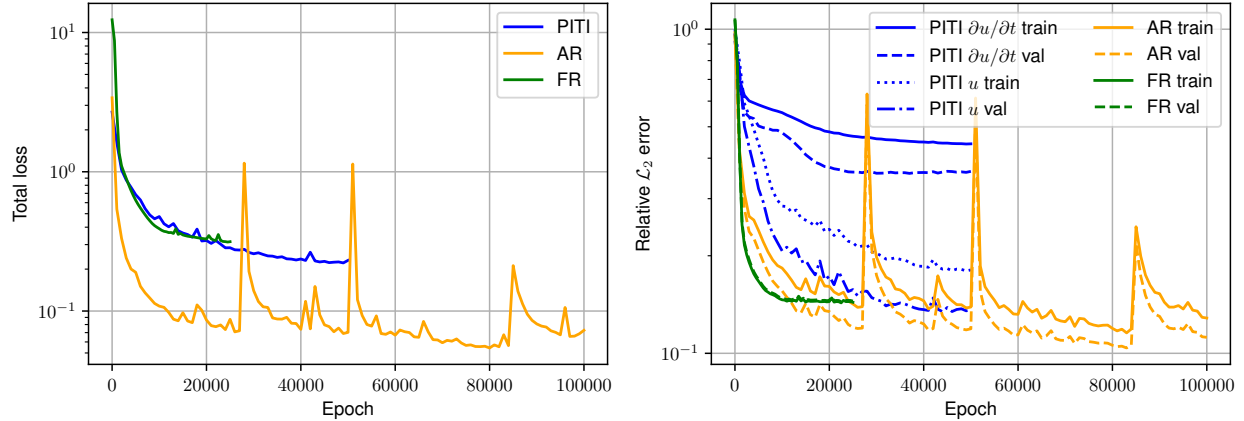


Figure 15: 2D Allen-Cahn equation: Total loss during training alongside mean relative \mathcal{L}_2 error on the train and validation set for full rollout (FR), autoregressive (AR), and time integration (PITI) model. The relative \mathcal{L}_2 error on both network outputs is provided for the PITI model. Hyperparameters were adapted per model as per table 2.

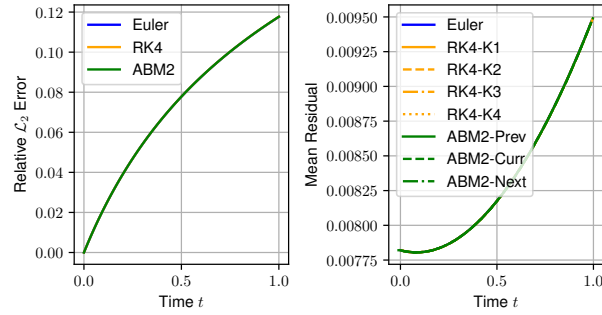


Figure 16: 2D Allen-Cahn equation: Comparison of different time integration (PITI) methods using explicit Euler, fourth-order Runge-Kutta (RK4) and second-order Adam-Bashforth-Moulton (ABM2) with mean relative \mathcal{L}_2 error on the left and predicted residuals on the right over all test examples.

In addition to the investigations described above and the network architectures explored during hyperparameter optimization, the final configurations were trained using five different random seeds. For evaluation, the relative \mathcal{L}_2 error was computed for each test sample, and its mean, minimum, and maximum were recorded at two representative time points: (i) the end of the training time horizon and (ii) the end of the test time horizon. Across the five seeded trainings, we report the grand mean and the between-seed standard deviation (formatted as $\mu \pm \sigma$) of these summary statistics in Table 4.

Overall, the between-seed standard deviations are typically at least one order of magnitude smaller than the corresponding error levels. In the remaining cases, the variability is either noticeably smaller while remaining within the same order of magnitude, or the absolute error is already sufficiently large that seed-induced variation is negligible in comparison. This indicates that the reported performance is robust with respect to the choice of random seed and that seed effects do not materially affect the conclusions drawn in the previous sections.

4 Discussion

PITI-DeepONet offers rapid, high-accuracy inference with limited to no training data as demonstrated by the numerical examples. Extrapolation using this method proves to be more stable and outperforms AR and FR methods, even extending far beyond the domain that was sampled for training: for the heat equation example up to 10 times the training domain. While the learned temporal tangent space operator incurs a higher inference cost compared to FR, it surpasses these methods in accuracy. We further explored different architectures for learning the temporal tangent space of time-evolution PDEs, but the results are similar to worse, while the presented architecture is the most general, being applicable to PDEs with mixed and/or higher-order derivatives in time and space. For the latter, one might

incorporate an additional consistency loss, although the optimization process may become more challenging. While not the focus of this study, the accuracy of our model depends on the reliability of AD, and it may be affected if AD produces unstable results.

The proposed method includes a built-in mechanism for tracking residuals during field reconstruction, providing an indicative measure of prediction quality at inference time. Across all examples, the residuals exhibited a nearly perfect linear correlation with the squared difference between predictions and the reference solutions obtained using explicit Euler, highlighting the strong error-monitoring capabilities inherent in the proposed PITI-DeepONet framework. This residual tracking approach enables additional possibilities, such as coupling it with more accurate schemes when a residual threshold is exceeded or facilitating active learning by identifying whether a state lies within the training domain. It can also serve as a time-step control criterion, allowing the rejection of a step if an unlearned or unexpected state arises, ensuring consistency in the inferred behavior.

A crucial aspect of effectively employing PITI-DeepONet is ensuring that all potential states encountered during inference are adequately sampled. These states can be obtained through experiments, traditional methods such as numerical or analytical solutions, or alternative surrogate models, such as FR simulations. Incorporating expert domain knowledge can significantly enhance the efficiency and quality of the sampling process. An additional, yet unexplored, avenue is the use of multi-fidelity learning [27], where data of varying resolutions or qualities can be seamlessly included within this framework. Moreover, it has been shown that a hybrid approach, which directly incorporates observed data, can greatly improve the learning process. However, this comes with the potential requirement of time derivative data for training, which may or may not be readily available, depending on the method used to acquire the data.

It is important to emphasize that no specific assumptions were made regarding the neural network architecture, allowing for the use of flexible, problem-specific designs. This can include architectures tailored to the number of variables, such as multi-input [28] and multi-output [29], as well as multi-network setups, i.e., a single network per field variable in coupled problems [30]. In this work, DeepONets with traditional feed-forward neural networks for the branch and trunk, as well as convolutional neural networks for the branch, were utilized; however, other (physics-informed) NO architectures are equally applicable. Furthermore, this framework can be readily scaled to higher-dimensional PDEs by adopting separable architectures [31].

5 Conclusion

In summary, a practical architecture, PITI-DeepONet, is presented that achieves long-term accuracy with reasonable inference time, enabling near real-time predictions while incurring only a marginal increase in computational cost compared to traditional operator learning methods. The proposed approach leverages physics-informed temporal tangent space learning with restricted sampling, exhibiting strong, reliable extrapolation capabilities. Although the current study focused on three academic benchmark problems, this method has the potential to transform surrogate operator learning by bridging the gap between data-driven/physics-informed learning and classical numerical solvers. As a natural next step, the approach will be extended to tackle more challenging and potentially chaotic/stiff PDE systems.

Acknowledgments

LM and TR were supported by Deutsche Forschungsgemeinschaft (DFG, German Research Foundation) by grant number 465194077 (Priority Programme SPP 2311, Project SimLivA) and under Germany’s Excellence Strategy – EXC 2075 – 390740016. TR thanks the Deutsche Forschungsgemeinschaft (DFG, German Research Foundation) for support via the project “Hybrid MOR” by grant number 504766766. TR is further supported by the Federal Ministry of Education and Research (BMBF, Germany) within ATLAS by grant number 031L0304A. LM is supported by the Add-on Fellowship of the Joachim Herz Foundation. The research efforts of DN and SG were partly supported by the National Science Foundation (NSF) under Grant No. 2438193 and 2436738. Any opinions, findings, conclusions, or recommendations expressed in this material are those of the author(s) and do not necessarily reflect the views of the funding organizations.

Author contributions

LM, DN, TR, and SG conceptualized this work. LM generated the data, implemented the training and inference schemes in software, and prepared results for analysis. LM, DN, and SG performed the formal analysis of the results. TR and SG supervised the project. LM, DN, and SG drafted the original manuscript, and all authors reviewed and edited the final version.

References

- [1] Lu Lu, Pengzhan Jin, Guofei Pang, Zhongqiang Zhang, and George Em Karniadakis. Learning nonlinear operators via DeepONet based on the universal approximation theorem of operators. *Nature machine intelligence*, 3 (3):218–229, 2021. doi: 10.1038/s42256-021-00302-5.
- [2] Zongyi Li, Nikola Borislavov Kovachki, Kamyar Azizzadenesheli, Burigede liu, Kaushik Bhattacharya, Andrew Stuart, and Anima Anandkumar. Fourier Neural Operator for Parametric Partial Differential Equations. In *In Proceedings of the International Conference on Learning Representations*, 2021.
- [3] Kazuma Kobayashi, James Daniell, and Syed Bahauddin Alam. Improved generalization with deep neural operators for engineering systems: Path towards digital twin. *Engineering Applications of Artificial Intelligence*, 131:107844, May 2024. ISSN 0952-1976. doi: 10.1016/j.engappai.2024.107844.
- [4] Vijay Kag, Dibakar Roy Sarkar, Birupaksha Pal, and Somdatta Goswami. Learning hidden physics and system parameters with deep operator networks, 2024. URL <https://arxiv.org/abs/2412.05133>.
- [5] Ning Liu, Xuxiao Li, Manoj R. Rajanna, Edward W. Reutzel, Brady Sawyer, Prahalada Rao, Jim Lua, Nam Phan, and Yue Yu. Deep neural operator enabled digital twin modeling for additive manufacturing. *Advances in Computational Science and Engineering*, 2(3):174–201, 2024. ISSN 2837-1739. doi: 10.3934/acse.2024010.
- [6] Shashank Kushwaha, Jaewan Park, Seid Koric, Junyan He, Iwona Jasiuk, and Diab Abueidda. Advanced deep operator networks to predict multiphysics solution fields in materials processing and additive manufacturing. *Additive Manufacturing*, 88:104266, May 2024. ISSN 2214-8604. doi: 10.1016/j.addma.2024.104266.
- [7] Kazuma Kobayashi and Syed Bahauddin Alam. Deep neural operator-driven real-time inference to enable digital twin solutions for nuclear energy systems. *Scientific Reports*, 14(1), January 2024. ISSN 2045-2322. doi: 10.1038/s41598-024-51984-x.
- [8] Somdatta Goswami, David S Li, Bruno V Rego, Marcos Latorre, Jay D Humphrey, and George Em Karniadakis. Neural operator learning of heterogeneous mechanobiological insults contributing to aortic aneurysms. *Journal of the Royal Society Interface*, 19(193):20220410, 2022. doi: 10.1098/rsif.2022.0410.
- [9] George Em Karniadakis, Ioannis G. Kevrekidis, Lu Lu, Paris Perdikaris, Sifan Wang, and Liu Yang. Physics-informed machine learning. *Nature Reviews Physics*, 3(6):422–440, May 2021. ISSN 2522-5820. doi: 10.1038/s42254-021-00314-5.
- [10] Sifan Wang, Hanwen Wang, and Paris Perdikaris. Learning the solution operator of parametric partial differential equations with physics-informed deeponets. *Science Advances*, 7(40), October 2021. ISSN 2375-2548. doi: 10.1126/sciadv.abi8605.
- [11] Somdatta Goswami, Aniruddha Bora, Yue Yu, and George Em Karniadakis. *Physics-Informed Deep Neural Operator Networks*, page 219–254. Springer International Publishing, 2023. ISBN 9783031366444. doi: 10.1007/978-3-031-36644-4_6.
- [12] Guang Lin, Christian Moya, and Zecheng Zhang. Learning the dynamical response of nonlinear non-autonomous dynamical systems with deep operator neural networks. *Engineering Applications of Artificial Intelligence*, 125:106689, 2023. doi: <https://doi.org/10.1016/j.engappai.2023.106689>.
- [13] Sifan Wang and Paris Perdikaris. Long-time integration of parametric evolution equations with physics-informed DeepONets. *Journal of Computational Physics*, 475:111855, 2023. doi: 10.1016/j.jcp.2022.111855.
- [14] Michael McCabe, Peter Harrington, Shashank Subramanian, and Jed Brown. Towards Stability of Autoregressive Neural Operators. *Transactions on Machine Learning Research*, 2023. ISSN 2835-8856. URL <https://openreview.net/forum?id=RFfUUtKYOG>.
- [15] Waleed Diab and Mohammed Al-Kobaisi. Temporal Neural Operator for Modeling Time-Dependent Physical Phenomena, 2025.
- [16] Katarzyna Michałowska, Somdatta Goswami, George Em Karniadakis, and Signe Riemer-Sørensen. Neural operator learning for long-time integration in dynamical systems with recurrent neural networks. In *2024 International Joint Conference on Neural Networks (IJCNN)*, pages 1–8. IEEE, 2024. doi: 10.1109/IJCNN60899.2024.10650331.
- [17] Ricardo Buitrago, Tanya Marwah, Albert Gu, and Andrej Risteski. On the benefits of memory for modeling time-dependent PDEs. In *International Conference on Learning Representations (ICLR)*, 2025. ICLR, 2024. URL <https://openreview.net/forum?id=o9kqa5K3tB>.
- [18] Junyan He, Shashank Kushwaha, Jaewan Park, Seid Koric, Diab Abueidda, and Iwona Jasiuk. Sequential deep operator networks (S-DeepONet) for predicting full-field solutions under time-dependent loads. *Engineering Applications of Artificial Intelligence*, 127:107258, 2024. doi: 10.1016/j.engappai.2023.107258.

- [19] Dibyajyoti Nayak and Somdatta Goswami. Ti-deeponet: Learnable time integration for stable long-term extrapolation, 2025.
- [20] Diederik P. Kingma and Jimmy Ba. Adam: A Method for Stochastic Optimization, 2017. URL <https://arxiv.org/abs/1412.6980>.
- [21] Takuya Akiba, Shotaro Sano, Toshihiko Yanase, Takeru Ohta, and Masanori Koyama. Optuna: A Next-Generation Hyperparameter Optimization Framework. In *The 25th ACM SIGKDD International Conference on Knowledge Discovery & Data Mining*, pages 2623–2631, 2019.
- [22] Zongren Zou, Zhicheng Wang, and George Em Karniadakis. Learning and discovering multiple solutions using physics-informed neural networks with random initialization and deep ensemble, 2025. URL <https://arxiv.org/abs/2503.06320>.
- [23] James Bradbury, Roy Frostig, Peter Hawkins, Matthew James Johnson, Chris Leary, Dougal Maclaurin, George Necula, Adam Paszke, Jake VanderPlas, Skye Wanderman-Milne, and Qiao Zhang. JAX: Composable transformations of Python+NumPy programs, 2018. URL <http://github.com/google/jax>.
- [24] Jonathan Heek, Anselm Levskaya, Avital Oliver, Marvin Ritter, Bertrand Rondepierre, Andreas Steiner, and Marc van Zee. Flax: A neural network library and ecosystem for JAX, 2023. URL <http://github.com/google/flax>.
- [25] DeepMind, Igor Babuschkin, Kate Baumli, Alison Bell, Surya Bhupatiraju, Jake Bruce, Peter Buchlovsky, David Budden, Trevor Cai, Aidan Clark, Ivo Danihelka, Antoine Dedieu, Claudio Fantacci, Jonathan Godwin, Chris Jones, Ross Hemsley, Tom Hennigan, Matteo Hessel, Shaobo Hou, Steven Kapturowski, Thomas Keck, Iurii Kemaev, Michael King, Markus Kunesch, Lena Martens, Hamza Merzic, Vladimir Mikulik, Tamara Norman, George Papamakarios, John Quan, Roman Ring, Francisco Ruiz, Alvaro Sanchez, Laurent Sartran, Rosalia Schneider, Eren Sezener, Stephen Spencer, Srivatsan Srinivasan, Miloš Stanojević, Wojciech Stokowiec, Luyu Wang, Guangyao Zhou, and Fabio Viola. The DeepMind JAX Ecosystem, 2020. URL <http://github.com/google-deepmind>.
- [26] Tobin A. Driscoll, Nicholas Hale, and Lloyd N. Trefethen. Chebfun Guide, 2014. URL https://www.chebfun.org/docs/guide/chebfun_guide.pdf.
- [27] Amanda A Howard, Mauro Perego, George Em Karniadakis, and Panos Stinis. Multifidelity deep operator networks for data-driven and physics-informed problems. *Journal of Computational Physics*, 493:112462, 2023. doi: 10.1016/j.jcp.2023.112462.
- [28] Pengzhan Jin, Shuai Meng, and Lu Lu. MIONet: Learning multiple-input operators via tensor product. *SIAM Journal on Scientific Computing*, 44(6):A3490–A3514, 2022. doi: 10.1137/22M1477751.
- [29] Lu Lu, Xuhui Meng, Shengze Cai, Zhiping Mao, Somdatta Goswami, Zhongqiang Zhang, and George Em Karniadakis. A comprehensive and fair comparison of two neural operators (with practical extensions) based on FAIR data. *Computer Methods in Applied Mechanics and Engineering*, 393:114778, April 2022. ISSN 0045-7825. doi: 10.1016/j.cma.2022.114778.
- [30] Shengze Cai, Zhicheng Wang, Lu Lu, Tamer A. Zaki, and George Em Karniadakis. DeepM&Mnet: Inferring the electroconvection multiphysics fields based on operator approximation by neural networks. *Journal of Computational Physics*, 436:110296, July 2021. ISSN 0021-9991. doi: 10.1016/j.jcp.2021.110296.
- [31] Luis Mandl, Somdatta Goswami, Lena Lambers, and Tim Ricken. Separable physics-informed DeepONet: Breaking the curse of dimensionality in physics-informed machine learning. *Computer Methods in Applied Mechanics and Engineering*, 434:117586, February 2025. ISSN 0045-7825. doi: 10.1016/j.cma.2024.117586.